S. Samanta, A. S. Nissimagoudar, R. Basori, A. Kuzmin, M. Li, J. Zhang, L. Wang, Y. Tian, H.-K. Mao, Unprecedented pressure-driven metallization and topological charge transport in an anion radical salt, Mater. Today Phys. 20 (2021) 100467. doi: 10.1016/j.mtphys.2021.100467.

Unprecedented Pressure-driven Metallization and Topological Charge Transport in an Anion Radical Salt

Sudeshna Samanta[2,3], Arun S Nissimagoudar[4], Rabaya Basori[5], Alexei Kuzmin[6], Mingtao Li[2], Jinbo Zhang[7], Lin Wang[1]*, Yongjun Tian[1], and Ho-kwang Mao[2]

[1] Center for High Pressure Science (ChiPS), State Key Laboratory of Metastable Materials Science and Technology, Yanshan University, Qinhuangdao, Hebei 066004, China.

[2] Center for High Pressure Science and Technology Advanced Research, Shanghai 201203, China.

[3] School of Information Science and Technology, Fudan University, Shanghai 200433, China.

[4] Center for Superfunctional Materials, Department of Chemistry, School of Natural Science, Ulsan National Institute of Science and Technology (UNIST), Ulsan 44919, Korea.

[5] School of Nanoscience and Technology, Indian Institute of Technology, Kharagpur 721302, India.

[6] Institute of Solid State Physics, University of Latvia, Riga 1063, Latvia.

[7] Department of Physics, Yangzhou University, Yangzhou 225009, China.

Key words: Topological charge transport, pressure-temperature phase-diagram, x- ray absorption, charge-transfer complex

*Corresponding author: **linwang@ysu.edu.cn**

S. Samanta, A. S. Nissimagoudar, R. Basori, A. Kuzmin, M. Li, J. Zhang, L. Wang, Y. Tian, H.-K. Mao, Unprecedented pressure-driven metallization and topological charge transport in an anion radical salt, Mater. Today Phys. 20 (2021) 100467. doi: 10.1016/j.mtphys.2021.100467.

Abstract

The hybrid inorganic/organic closed π-stacking and soft lattice of a copper anion radial (copper-7,7,8,8-tetracyanoquinododimethane) renders its electrical conductivity and structural modifications, which are susceptible to temperature and pressure. The geometry of its metal-ligand construction contemplates the concept of topology with a charge-transfer instability. A pressure-induced ionic-neutral phase transition occurs and accompanies an anomalously large electrical conductivity, carries topological charges, and possesses a low energy gap smaller than the Coulomb gap. X-ray absorption spectroscopy of the metal establishes the high electrical conduction by the topological charges. X-ray diffraction and the first-principles calculations further suggest that the compression leads to an irreversible alteration in the metal coordination and rotation of the quinoid rings of the anion. The present observation demonstrates a close coupling of topological charges and lattice dynamics within a relatively low-pressure regime, which may expand a novel paradigm for the comprehensive topological charge transport phenomena including thermoelectric effects in future.

INTRODUCTION

In contrast to inorganic metals, the crystals of organic charge-transfer complexes with ordered stacked radicals present closed-shell structure with small transfer integral and large onsite Coulomb repulsion energy U coupled to their charge transport. Moreover, they have intermolecular orbital overlap resulting in an extremely narrow electronic bandwidth W. Thus, a large U/W ratio compels the radial based system to remain trapped in a Mott insulating state with unpaired isolated electrons [1-3]. Electronic criteria to advance the charge transport is conceptually simple, but practically challenging. Hubbard model predicts a metallic ground state based on a half-filled band ($s = 1/2$ system) must require $W > U$, as observed in few highly conductive frameworks [3]. An alternative approach is to include heavy heteroatom in radical-based materials that satisfies $W > U$. This inclusion inevitably increases the tendency of dimerization and leads to a subsequent quenching of spin and charge carriers which further results in a Peierls distorted insulating or weakly semiconducting ground state [4]. Hence, the challenge that persists for improvements in conductivity requires to reduce U, increase W, and prevent dimerization.

The charge transfer (CT) compounds are appealing because, under compression with gigapascal pressures, they exhibit dramatic modifications of electronic and structural states of matter [5-13]. Indeed, compression increases intermolecular interaction, contracts the lattice, and originates a local potential which intends to localize the electrons. Such a self-trapping phenomenon is enabling comprehensive views into the basic electron-phonon coupling (EPC) process where

pressure probes EPC and its localization mechanism. The electronic response of CT compounds ranges from strong EPC (insulating) to weak EPC (metallic) mechanisms. However, the intermediate coupling (IC) range remains highly intriguing and demonstrates insulator- or semiconductor-metal transition (IMT or SMT) where pressure modifies the transition temperature by forcing effective ($W_{eff} \propto T_{IM}$) to change.

The quasi-one dimensional π-stack anion radical complex like copper-7,7,8,8-tetracyanoquinododimethane (Cu-TCNQ) [14-16] is a prototype CT compound which exhibits semiconducting ground state along with a Peierls distortion [17, 18] at low temperature. Apart from its advanced applications[19, 20], we successfully reveal a pressure-driven metallization process by tuning the degree of band occupation (lower U and increase W) accompanying an ionic-neutral phase transition. In the ionic phase, cations possess a fully occupied electron shell without any spin state. Across the phase transition to the neutral state, the spin degrees of freedom could be activated under pressure by spin-singlet formation in absence of dimerization. Therefore, we argue that pressure subsequently triggers the emergence of current carrying topological excitons [21]. The presence of such excitons in form of neutral anions (A^0) was reported in tetrathiafuvalene-p- chloranil (TTF-CA) crystal [22] where photoexcitation created “excess charge” and delocalized. Therefore, the increase of conductivity with low temperature and pressure in Cu-TCNQ may involve the propagation of charge and spin solitons with a subtle balance of fluctuations between lattice and electronic energies. Considering its general softness

(elasticity and high compressibility) and allowing the thermodynamic responses (phase stability and transition), the exotic electronic properties of this CT compound can organize an interesting platform to study its structural and physical properties under external hydrostatic pressure.

RESULTS

Enhancement of electrical conductivity and semiconductor-to-metal transition

We sealed Cu-TCNQ nanowires along with the platinum (Pt) electrodes in a diamond-anvil-cell (DAC) to perform in-situ quasi-hydrostatic pressure dependent studies. They demonstrate a wide range of physical properties as a response to pressure, and electrical conductivity is one of them. First, we present a pressure-temperature ($P-T$) phase diagram in Fig. 1(a) up to 30 GPa constructed on the basis of resistivity ($R-T$) profiles in Fig. 1(b). These profiles are distinctly different below and above 0.7 GPa. Below 0.7 GPa, a strong insulating behavior is pronounced at low temperature indicating the presence of a large and robust charge gap against pressure. For pressures above 0.7 GPa, the ambient semiconducting state is gradually suppressed and SMT occurs at temperature T_{SE} defined by the kink in $R-T$ curve (Fig. 1(b): inset). A contour plot of the resistivity (Fig. 1(a)) illustrates an emergence of highly conducting state. The resistivity steeply rises for $T < T_{SE}$ where SMT only visible at high temperatures 240 K $< T <$ 300K and survives up to 13 GPa. For this narrow temperature region, resistance follows power-law behavior $R(T) \propto T^{\varsigma}$ with $0 < \varsigma < 1$ and rules out the possibility of the Fermi liquid ($\varsigma = 2$) and Bloch-Grüneisen theory of electron-phonon scattering $\varsigma = 1$. The shifting of T_{SE}towards the

low temperature with increasing pressure clearly infers about a significant contribution from the pressure-driven weakening of EPC, i.e., considerable broadening of W_{eff}. The conduction mechanism is further characterized by the Efros-Shklovskii variable range hopping (ESVRH) model (Fig. 1(c)) as $R = R_0 \exp\left[\left(\frac{T_0}{T}\right)^{1/2}\right]$ where $T_0 = 2.8e^2/(\epsilon k_B \xi)$ is the ESVRH characteristic temperature as coupled to the localization length (ξ) and dielectric constant (ϵ) of the material [23]. In typical semiconductors, ξ grows (Fig. 1(d)) with the increasing electron concentration n and reduces T_0. Here, T_0 reaches to the minimum around 10 GPa (Fig. 1(c): inset). Fig. 2 shows the pressure dependence of resistivity expressed in terms of current-voltage $(I-V)$ characteristics and illustrates that a highly conducting state is appearing around 10 GPa. The compression-induced non-linear conductivity demonstrates an ON-state with a strikingly high current ~ 10^2 mA for a low applied pressure ~ 1.0 GPa (Fig. 1(a)) (Supplementary Materials: Section S1 and Fig. S1(a)). For a critical pressure P_c =1.1 GPa and positive (negative) bias sweep, current rapidly switches from an OFF-state (HRS: high resistive state) to an ON-state (LRS: low resistive state) at a threshold voltage V_{SET} (V_{RESET}). It is remarkable that the conductivity is enhanced by ~ 10^3 (10^2) times from its ambient value at 1.0 (0.5) GPa even with a low applied bias (Fig. 2(b)) for Cu-TCNQ phase-I (phase-II, Supplementary Materials: Fig. S1).

The conductivity rises steeply up to 8.0-9.0 GPa and a high-conducting state sustains without any distinct ON-OFF states (Fig. 2(b)). The pressure-driven SMT (conductivity maximum in Fig. 1(c)) indicates that donor to acceptor charge transfer

is not only confined in the transition region, but also defined by the nature of the bonds. In comparison with other alkali-metal-TCNQ salts [24], Cu-TCNQ phase-I demonstrates the lowest transition pressure for SMT (Fig. 2(c): inset). Phase-II converts to phase-I *via* an unstable phase-III [25] at the expense of bond breakage, their rearrangements, and a formation of new Cu-N coordination bonds and therefore, delays the transition [16]. Due to organic-framework's soft nature, application of ultra-high pressure causes an irreversible change in it; thus fails to regain the original structure and conductivity starts to decrease significantly above 12 GPa (16 GPa, phase-II) (Fig. 2(c)). The recovery of conductivity after pressure release on Cu-TCNQ structures is only applicable below SMT.

Coulomb gap and charge localization

At ambient pressure and T <100 K, non-linear conductance and a CDW transport was manifested by Peierls transitions [17]. We observed that the exchange of energy between lattice and electrons promotes the delocalization of carriers and thus explains the high conducting states [26]. The improved nanoscopic intra- ($t_{||}$) and inter-molecular ($t_{\perp}$) transfer integrals between the donor and acceptor molecules clearly explain the weaker localization with reduction of T_0 which is further reduced to Coulomb gap $\Delta_{CG} = k_B\sqrt{T_0 T_{SE}}$ at Fermi level (Fig. 1(d)). We assume ESVRH conduction process emerges at the temperature T_{SE} whenactivation energy for nearest neighbor hoping becomes equal to Δ_{CG}. An exponential shrinkage of Δ_{CG} assures the highest conductivity around 10 GPa.

There might exist different transfer integrals between the nearest neighbor chains (t_1: Cu-4N$_1$ and t_2: Cu-2N$_2$) and the system remains trapped to the insulating state for $t_1 = t_2 = 0$. For a large value of t_{12} (Cu-6N), charge gap collapses, and a metallic state emerges. A more rigorous calculation of ξ connects the hopping length as $l_h = (\xi/4)(T_0/T)^{1/2}$ yielding an estimated l_h (20 K, 10 GPa) ~ 12 nm. Taking carrier density n_{CuTCNQ} = 2.34×10^{24}/m^3, the mean distance between two hopping sites is $\frac{\langle r \rangle}{2} = \left[3/\left(4\pi n_{CuTCNQ}\right)\right]^{1/3}$ ~ 1 nm. At the lowest possible temperature, $\langle r \rangle$ is of the same order with signifying the electron localizations below T_{SE}. The long-range Coulomb interactions of the localized electrons could only create a soft energy gap for low pressure and temperature $T < T_{SE}$. For P >14 GPa, the structural disorders and later pressure-induced amorphization (PIA) strengthen the localization effects, make the EPC stronger, and revive an insulating state. However, it might be hard to achieve a metallic ground state (0 K) without destroying the molecular structure.

Pressure effect on the local atomic and electronic structure

Synchrotron X-ray absorption spectroscopy (XAS) in Fig.3 reveals the chemical state and coordination geometry in Cu-TCNQ at room temperature. The Cu K-edge of X-ray absorption near-edge structures (XANES) in Cu-TCNQ at low pressures (5 and 9 GPa) exhibit a distinct peak at about 8981.5 eV attributed to the dipole- allowed Cu 1s $\rightarrow$ 4p transition [27]. At larger pressures, the peak is masked by the overlapping EXAFS oscillations due to the pressure-induced changes in the atomic structure upon

amorphization (Fig. 3(a)). The position of the copper absorption edge determined as a first derivative of the absorption coefficient shifts by about 0.5 eV to lower binding energies upon compression (Fig. 3(a): inset). Therefore, it suggests a slight decrease in the copper oxidation state from Cu^{+} towards Cu^{0} due to the changes in the overall charge density under compression [28]. Note that even at the highest pressure of 27.8 GPa, the position of the copper edge for Cu-TCNQ is located about 1 eV above the edge for the reference copper foil.

The pressure-dependence of the EXAFS oscillations (Fig. 3(b)) indicate that the main EXAFS frequency, determined by the nearest atoms, remains nearly unchanged. The high-frequency contributions due to the next groups of atoms vary significantly, especially at the highest pressure of 27.8 GPa. These effects can be better evidenced in the *R*-space (Fig. 3(c)), where pressure-induced changes of interatomic distances are clearly visible. While the first peak position remains unchanged at all pressures, the second one shifts from about 2.6 Å to 2.3 Å upon increasing pressure to 27.8 GPa. In a highly distorted tetrahedral environment[14], the nitrogen atoms (N_1) are the main responsible for the first peak in FTs. Other two nitrogen atoms (N_2) and four carbons (C_3) located at longer distances contribute to the first and second peaks in FTs, respectively. The pressure dependence of the average interatomic distances R(Cu-N_1), R(Cu-N_2), and R(Cu-C_3) obtained from the best-fit analysis is reported in Fig. 3(d). Both groups of the Cu-N bonds demonstrate weak dependence on pressure; however, the Cu-C bonds become compressed at $P > 10$ GPa. Such behavior of interatomic distances suggests that nitrogen atoms play the role of joints allowing TCNQ ligands to rotate under compression. It may

also allow distortion of the framework or modification in metal center coordination accompanying successive phase transitions to lower symmetric phases from its ambient monoclinic *Pn* phase (Supplementary Materials: Fig. S2, Fig. S3, and Fig. S4). Pressure-induced volume reduction in Fig.4 (a) occurs due to a steep reduction of c -axis (ease of compression of π-stacks) compared to a monotonic decrease of a and b axes (Fig. 4(b)). The in-plane closely packed C≡N bonds along $a - b$ planes may accommodate a greater compression resulting in an anisotropic compression in the lattice.

Coordination of donor atoms, change in bond order, and charge transfer

By comparing the three molecular structures (Fig. 1(a)), the drastic pore volume reduction necessitates the accommodation of tilting/distortion of the metal coordination polyhedral confirmed by the cation coordination changes from tetrahedral to octahedral (Fig. 1(a)) around 8.7 GPa. In this denser phase, the average Cu-N_1 distance is 2.09 Å consistent with previous reports [16]. The two nearest N-atoms coordinated to the Cu-site are at the shortest distance of 1.91 Å, while the C-C bonds are strongly bent, but the C-rings remain parallel at 3.47 Å apart. The vibrational modes corresponding C=C-H bending and C-C≡N stretching frequencies (Supplementary Materials: Fig. S5) demonstrate distinct changes with pressure and the population of electrons in TCNQ increases with decreasing lengths of these bonds [29, 30]. Their dominant role in electrical conductivity is estimated by the degree of charge transfer (DCT) from donors to acceptors and is a linear correlation with cyano-vibrational mode as $DCT = 2(\delta\nu/\nu_0)(1 - \nu_1^2/\nu_0^2)$ where $\delta\nu = \nu_0 - \nu_{CT}$, and ν_0,

ν_{CT}, ν_1 represent selective stretching modes of a pure acceptor, charge transfer compound, and acceptor anion respectively. The fractional DCT =0.5 at ambient condition with localized electrons within frameworks decreases with pressure (Supplementary Materials: Fig. S6). The exocyclic double bonds become short and reduce their bond order due to the loss of certain degrees of rotational freedom under compression [16]. The anisotropic repercussions of unit cell contraction are likely to encompass a disruption of the CT mechanism in the approach of orbital overlap and preference of the neutral states of Cu^0 and $TCNQ^0$ (Fig. 4(a)).

Electronic band structure and collapse of band gap

The projected density of states (PDOS) and the electronic band structure are displayed in Fig 5 shows the valence band maxima (VBM) crosses the Fermi level for all pressures considered. The result is highly consistent with earlier theoretical investigation [15] at ambient condition. In PDOS, Cu-3d, C-2p and N-2p orbitals form VBM, whereas contribution to CBM comes from C-2p and N-2p orbitals (Fig. 5(a) and Fig. S7). Demonstrating an indirect to direct band gap transition, the experimental (theoretical) band gap shows a red shift up to cross over region around 11.7 GPa and reaches to its minimum value ~ 1.3 (0.8) eV (Fig. 5(b)). It also confirms the emergence of a metallic state under pressure. A strong compression leads to highly distorted structure, bending of chemical bonds, fragmentation of organic layers, and successive lower symmetric structural transitions. Therefore, few available energy states are available to support an indirect band gap at high pressure.

DISCUSSION

Our results provide insights into topological charge transport

Cu-TCNQ is a radical anion salt and displays a strong ionic character at ambient condition[14, 15] and the cation has fully occupied electron shell (no spin), whereas the lowest unoccupied molecular orbital (LUMO) of TCNQ molecule is empty. They possess segregated donor (D) and acceptor (A) stacks with partial charge transfer from donor Cu to acceptor TCNQ schematically depicted in Fig. 6(a). The partial charge transfer from Cu to TCNQ occurs due to strong hybridization of the orbitals and a semiconducting state with low-bandwidth prevails. However, upon compression, shrinkage of lattice and bond lengths corroborate significant broadening of the bandwidth and consequent redshift of the band gap (Fig. 5) at ambient temperature. However, to explain the emergence of metallic states at low pressure and relatively high temperature ($T > T_{SE}$), we propose the generation of topological excitations. They are solitons; they become active and competes with structural fluctuations resulting a decrease (increase) of resistance (conductivity) (Fig. 2(b)). These current-carrying topological charges are originating from a charge inhomogeneity at the critical pressure P_C ~1 GPa (Fig. 3(a)) and can be excited with relatively lower excitation energies than Δ_{CG}. Therefore, few $TCNQ^-$ anions may convert to neutral $TCNQ^0$ and start to propagate along $TCNQ^-$ columns as solitons and carry charge as shown in Fig 6(b). The growing overlap among the wave functions of organic chains leads to the enhancement of the diffusive motion of the solitons and exhibits an increase of conductivity. The charge delocalization stabilizes

with further compression [16] and ambient semiconducting phase is gradually suppressed.

As it was experimentally demonstrated, Cu^{+} converts to the neutral Cu^{0} around 10 GPa (Fig. 4(a)), the spin solitons develop in the high pressure phase. In the adjacent chains, a charge (spin) soliton can hop into a spin (charge) soliton site by donating electrons with a high d.c current (Fig. 2(a)). Recently, ^{13}C-NMR (nuclear magnetic resonance) shift and relaxation rate (T_1^{-1}) analyses in TTF-CA also verified pressure-evolution of topological excitations like kinks at the paraelectric-ferroelectric (neutral-ionic (NI)) mobile domain walls (DWs) and charge-/spin-carrying solitons [31]. The authors proposed that sparsely excited spin solitons act like free spins in presence of negligible exchange interaction. A schematic in Fig. 6(c) demonstrates the spin soliton excitation in D-A pairs in the SMT region for Cu-TCNQ. Thus, at low pressure, the conductivity is ruled by charge solitons and is handed over to conductivity by spin solitons (below12 GPa). In TTF-CA [31], spin-solitons (polarons) sandwiched by NIDWs propagate in low- pressure neutral phase, while more densely charge solitons excited in high-pressure ionic phase. However, for both cases, the charge fluctuations are sensitive to thermal environment, and the occurrence of charge solitons decreases with decrease of temperature. Additionally, compression-induced lattice shrinkage couple the ($\pm$) soliton pairs (Fig. 6(d)) which do not find suitable way to hop in the adjacent stacks; and conductivity starts to decrease again.

The principles described here possible to apply more broadly

We unveiled a metallization process at low temperature and high pressure across an ionic-neutral phase transition in Cu-TCNQ. Pressure effectively tunes the EPC and reduces the U/W ratio significantly. Simple modeling and multimodal experiments conclude that the high conducting state via mobile topological excitons is enhanced under compression, in contrary to previous conventional electrical transport studies in metal-organic frameworks. Therefore, the interplay of lattice dynamics and pressure tuning of such transport paves way to a wide range of remarkable charge transport mechanisms. For example, it may be applicable to the recent development of the topological spin-dependent high performance new thermoelectric materials with interconnected nanowire networks [32].

MATERIALS AND METHODS

Sample Preparation

The single crystalline Cu-TCNQ nanowires were synthesized by physical vapor deposition technique (Fig. S8). It can be derived into two stable structures (Fig. S9) as phase-I (monoclinic-*Pn*) and phase-II (monoclinic-*P2/n*) with high (0.25 S-cm^{-1}) and low (1.3×10^{-5} S-cm^{-1}) conductivities.

In-Situ High Pressure experiments

Electrical transport: In-situ high-pressure electrical conductivity was measured with a four-probe direct-current (d.c) method at ambient temperature in a symmetric DAC. The low-temperature electrical transport measurements were carried out in Physical

Property Measurement System (PPMS) using Be-Cu screw drive DAC. The insulation between conducting leads and gaskets for both types were secured by compressing cubic boron nitride in the sample chamber. Thin platinum foils were used as conducting electrodes. No pressure transmitting medium (PTM) was used.

Structural characterizations: *In-situ* high-pressure synchrotron XRD experiments were conducted at ambient temperature at Shanghai Synchrotron Radiation Facilities (15U beamline with wavelength 0.6199 Å). A steel gasket (thickness ~ 40 μm, hole diameter 100 μm) and silicone oil was used as a PTM for the sample chamber. The 2-dimensional XRD data were integrated into one- dimensional profiles using the Dioptas program [33]. Le Bail fittings were carried out using the Jana2006 program [34] (Supplementary Materials: Section S2). The scanning electron microscopy image (Fig. S10) of recovered sample shows the change in packing density and increased dimensionality [35].

The high-pressure synchrotron x-ray absorption spectroscopy (XAS) experiments were performed at SPring-8 (BL05XU beamline). The synchrotron radiation from the in-vacuum undulator was monochromatized by a Si(111) monochromator, and higher harmonic X-rays were removed using Rh-coated mirrors. The energy scale was calibrated using copper foil. The sample was loaded without PTM in the DAC and was located between two ionization chambers. The Cu K-edge absorption spectra were collected in the transmission mode. The XAS data were analyzed by ATHENA [36] and XAESA [37] programs. The EXAFS spectra (Fig. 3(b)) were defined as after background

removal where is the photoelectron wavenumber, is a smoothly varying absorption background, and is the absorption edge-jump. Their Fourier transforms (FTs) were calculated using the 10% Gaussian window-function (Fig. 3(c)). The contribution from the nearest atoms (6N and 4C) around the absorbing copper was isolated by back-FT in the range of R=0.8-3.0 Å and analyzed within the single-scattering harmonic approximation using the conventional EXAFS equation [38] (Support information: Section S3, Fig. S11)

Raman and UV-vis spectroscopy

Raman spectra were recorded with a Raman spectrometer (Ranishaw, model: inVia micro-Raman) equipped with a 633 nm HeNe laser (17 mW) and 1800 l/cm grating.

The high-resolution pressure-induced UV-vis spectroscopy measurements were carried out using a micro UV-vis spectroscopy system (DH-2000-BAL, Ocean Optics) using a symmetric DAC with type-II diamonds.

The pressure was calibrated by the regular ruby fluorescence method for all pressure-dependent studies.

Theoretical electronic band structure calculations

Spin-polarized density functional theory (DFT) calculations were performed using the plane-wave formalism as implemented in the Quantum-Espresso package [39] with the norm-conserving pseudopotentials [40, 41]. We use generalized gradient

approximation (GGA) with Perdew–Burke-Ernzerhof (PBE) [42] exchange and correlation functional. The core–valence interaction was described by the projector-augmented wave method and the Van der Waals dispersion correction of Grimme [43] was considered. Plane wave functions were expanded with an energy cutoff of 100 Ry and Brillouin zone sampled using 15×15×15 gamma centered - mesh. Structural relaxation was performed by fixing the lattice parameters to the experimental results and all atoms were fully relaxed (Supplementary Materials: Fig. S8 (c)).

REFERENCES AND NOTES

[1] H. Kojima, Z. Zhang, K.R. Dunbar, T. Mori, Energy band structure and metal-organic interactions in tetracyanoquinodimethane (TCNQ) and N,N'-dicyanoquinonediimine (DCNQI) materials, Journal of Materials Chemistry C, 1 (2013) 1781-1790.

[2] M. Mitrano, G. Cotugno, S.R. Clark, R. Singla, S. Kaiser, J. Stahler, R. Beyer, M. Dressel, L. Baldassarre, D. Nicoletti, A. Perucchi, T. Hasegawa, H. Okamoto, D. Jaksch, A. Cavalleri, Pressure-dependent relaxation in the photoexcited mott insulator ET-F2TCNQ: influence of hopping and correlations on quasiparticle recombination rates, Phys Rev Lett, 112 (2014) 117801.

[3] Y. Yoshida, H. Kitagawa, One-dimensional electronic systems: metal-chain complexes and organic conductors, Chem Commun (Camb), 56 (2020) 10100-10112.

[4] R.E. Peierls, Quantum Theory of Solids, Oxford University Press: London, 2001.

[5] H. Cui, T. Tsumuraya, T. Miyazaki, Y. Okano, R. Kato, Pressure-Induced Metallic Conductivity in the Single-Component Molecular Crystal [Ni(dmit)2], European Journal of Inorganic Chemistry, 2014 (2014) 3837-3840.

[6] D.S. Chow, P. Wzietek, D. Fogliatti, B. Alavi, D.J. Tantillo, C.A. Merlic, S.E. Brown, Singular Behavior in the Pressure-Tuned Competition between Spin-Peierls and Antiferromagnetic Ground States of (TMTTF)2PF6, Physical Review Letters, 81 (1998) 3984-3987.

[7] J.W.L. Wong, A. Mailman, K. Lekin, S.M. Winter, W. Yong, J. Zhao, S.V. Garimella, J.S. Tse, R.A. Secco, S. Desgreniers, Y. Ohishi, F. Borondics, R.T. Oakley, Pressure Induced Phase Transitions and Metallization of a Neutral Radical Conductor, Journal of the American Chemical Society, 136 (2014) 1070-1081.

[8] A. Andrieux, H.J. Schulz, D. Jerome, K. Bechgaard, Conductivity of the One-Dimensional Conductor Tetrathiafulvalene-Tetracyanoquinodimethane (TTF-TCNQ) near Commensurability, Physical Review Letters, 43 (1979) 227-230.

[9] A. Jaffe, Y. Lin, W.L. Mao, H.I. Karunadasa, Pressure-induced conductivity and yellow-to-black piezochromism in a layered Cu-Cl hybrid perovskite, Journal of American Chemical Society, 137 (2015) 1673-1678.

[10] Q. Sui, X.T. Ren, Y.X. Dai, K. Wang, W.T. Li, T. Gong, J.J. Fang, B. Zou, E.Q. Gao, L. Wang, Piezochromism and hydrochromism through electron transfer: new stories for viologen materials, Chem Sci, 8 (2017) 2758- 2768.
[11] K.W. Chapman, G.J. Halder, P.J. Chupas, Pressure-Induced Amorphization and Porosity Modification in a Metal−Organic Framework, Journal of the American Chemical Society, 131 (2009) 17546-17547.
[12] F.-X. Coudert, Responsive Metal–Organic Frameworks and Framework Materials: Under Pressure, Taking the Heat, in the Spotlight, with Friends, Chemistry of Materials, 27 (2015) 1905-1916.
[13] S. Wang, Q. Wang, X. Feng, B. Wang, L. Yang, Explosives in the Cage: Metal-Organic Frameworks for High-Energy Materials Sensing and Desensitization, Adv Mater, 29 (2017).
[14] R.A. Heintz, H. Zhao, X. Ouyang, G. Grandinetti, J. Cowen, K.R. Dunbar, New Insight into the Nature of Cu(TCNQ): Solution Routes to Two Distinct Polymorphs and Their Relationship to Crystalline Films That Display Bistable Switching Behavior, Inorganic Chemistry, 38 (1999) 144-156.
[15] M.J. Capitan, J. Alvarez, F. Yndurain, Organometallic MTCNQ films: a comparative study of CuTCNQ versus AgTCNQ, Physical Chemistry Chemical Physics, 20 (2018) 21705-21715.
[16] R. Caputo, S. Demir, A. Tekin, First-Principles Crystal Structure Prediction of Cu(I)-TCNQ Polymorphs, The Journal of Physical Chemistry C, 124 (2019) 70-82.
[17] R. Basori, A.K. Raychaudhuri, Low temperature transport of a charge transfer complex nanowire grown with an electric field from the vapour phase, RSC Advances, 5 (2015) 86497-86504.
[18] M. Kumar, B.J. Topham, R. Yu, Q.B.D. Ha, Z.G. Soos, Magnetic susceptibility of alkali-tetracyanoquinodimethane salts and extended Hubbard models with bond order and charge density wave phases, The Journal of Chemical Physics, 134 (2011) 234304.
[19] R.S. Potember, T.O. Poehler, R.C. Benson, Optical switching in semiconductor organic thin films, Applied Physics Letters, 41 (1982) 548-550.
[20] R. Basori, K. Das, P. Kumar, K.S. Narayan, A.K. Raychaudhuri, Large photoresponse of Cu:7,7,8,8-tetracyanoquinodimethane nanowire arrays formed as aligned nanobridges, Applied Physics Letters, 102 (2013) 061111.
[21] J.L. Bredas, B. Themans, J.M. Andre, R.R. Chance, R. Silbey, The role of mobile organic radicals and ions (solitons, polarons and bipolarons) in the transport properties of doped conjugated polymers, Synthetic Metals, 9 (1984) 265-274.
[22] T. Suzuki, T. Sakamaki, K. Tanimura, S. Koshihara, Y. Tokura, Ionic-to-neutral phase transformation induced by photoexcitation of the charge-transfer band in tetrathiafulvalene-p-chloranil crystals, Physical Review B, 60 (1999) 6191-6193.
[23] S. Samanta, A.K. Raychaudhuri, Y.M. Mukhovskii, Non-Gaussian resistance noise in the ferromagnetic insulating state of a hole-doped manganite, Physical Review B, 85 (2012) 045127
[24] I. Shirotani, A. Onodera, N. Sakai, Electrical Behavior of Alkali Metal Cation–TCNQ Anion Radical Simple Salts under Very High Pressures, Bulletin of the Chemical Society of Japan, 48 (1975) 167-170.
[25] C.A. Fernandez, P.C. Martin, T. Schaef, M.E. Bowden, P.K. Thallapally, L. Dang, W. Xu, X. Chen, B.P. McGrail, An electrically switchable metal-organic framework, Sci Rep, 4 (2014) 6114.
[26] S. Yasuzuka, K. Murata, T. Arimoto, R. Kato, Temperature-Pressure Phase Diagram in TTF-TCNQ: Strong Suppression of Charge-Density-Wave State under Extremely High Pressure, Journal of the Physical Society of Japan, 76 (2007) 033701-033701.
[27] B. You, X. Liu, G. Hu, S. Gul, J. Yano, D.-e. Jiang, Y. Sun, Universal Surface Engineering of Transition Metals for Superior Electrocatalytic Hydrogen Evolution in Neutral Water, Journal of the American Chemical Society, 139 (2017) 12283-12290.
[28] A.I. Frenkel, Q. Wang, N. Marinkovic, J.G. Chen, L. Barrio, R. Si, A.L. Cámara, A.M. Estrella, J.A. Rodriguez, J.C. Hanson, Combining X-ray Absorption and X-ray Diffraction Techniques for in Situ Studies of Chemical Transformations in Heterogeneous Catalysis: Advantages and Limitations, The Journal of Physical Chemistry C, 115 (2011) 17884-17890.

[29] H. Jiang, P. Hu, J. Ye, K.K. Zhang, Y. Long, W. Hu, C. Kloc, Tuning of the degree of charge transfer and the electronic properties in organic binary compounds by crystal engineering: a perspective, Journal of Materials Chemistry C, 6 (2018) 1884-1902.
[30] C. Sun, H. Zhao, C. Liu, M. Zhou, Pressure-induced Fermi resonance between fundamental modes in 7,7,8,8-tetracyanoquinodimethane, Journal of Raman Spectroscopy, 48 (2017) 1127-1131.
[31] R. Takehara, K. Sunami, K. Miyagawa, T. Miyamoto, H. Okamoto, S. Horiuchi, R. Kato, K. Kanoda, Topological charge transport by mobile dielectric-ferroelectric domain walls, Science Advances, 5 (2019) eaax8720.
[32] N. Marchal, T. da Camara Santa Clara Gomes, F. Abreu Araujo, L. Piraux, Large Spin-Dependent Thermoelectric Effects in NiFe-based Interconnected Nanowire Networks, Nanoscale research letters, 15 (2020) 137.
[33] C. Prescher, V.B. Prakapenka, DIOPTAS: a program for reduction of two-dimensional X-ray diffraction data and data exploration, High Pressure Research, 35 (2015) 223-230.
[34] P. Václav, D. Michal, P. Lukáš, Crystallographic Computing System JANA2006: General features, Zeitschrift für Kristallographie - Crystalline Materials, 229 (2014) 345-352.
[35] S. Samanta, Q. Li, B. Cheng, Y. Huang, C. Pei, Q. Wang, Y. Ma, L. Wang, Phase coexistence and pressure-temperature phase evolution of VO_2{A) nanorods near the semiconductor-semiconductor transition, Physical Review B, 95 (2017) 045135.
[36] B. Ravel, M. Newville, ATHENA, ARTEMIS, HEPHAESTUS: data analysis for X-ray absorption spectroscopy using IFEFFIT, Journal of Synchrotron Radiation, 12 (2005) 537-541.
[37] A. Kalinko, XAESA v0.03, https://github.com/aklnk/xaesa (2020).
[38] A. Kuzmin, J. Chaboy, EXAFS and XANES analysis of oxides at the nanoscale, IUCrJ, 1 (2014) 571-589.
[39] P. Giannozzi, S. Baroni, N. Bonini, M. Calandra, R. Car, C. Cavazzoni, D. Ceresoli, G.L. Chiarotti, M. Cococcioni, I. Dabo, A. Dal Corso, S. de Gironcoli, S. Fabris, G. Fratesi, R. Gebauer, U. Gerstmann, C. Gougoussis, A. Kokalj, M. Lazzeri, L. Martin-Samos, N. Marzari, F. Mauri, R. Mazzarello, S. Paolini, A. Pasquarello, L. Paulatto, C. Sbraccia, S. Scandolo, G. Sclauzero, A.P. Seitsonen, A. Smogunov, P. Umari, R.M. Wentzcovitch, QUANTUM ESPRESSO: a modular and open-source software project for quantum simulations of materials, Journal of Physics: Condensed Matter, 21 (2009) 395502.
[40] D.R. Hamann, Optimized norm-conserving Vanderbilt pseudopotentials, Physical Review B, 88 (2013) 085117.
[41] P. Scherpelz, M. Govoni, I. Hamada, G. Galli, Implementation and Validation of Fully Relativistic GW Calculations: Spin–Orbit Coupling in Molecules, Nanocrystals, and Solids, Journal of Chemical Theory and Computation, 12 (2016) 3523-3544.
[42] J.P. Perdew, K. Burke, M. Ernzerhof, Generalized Gradient Approximation Made Simple, Physical Review Letters, 77 (1996) 3865-3868.
[43] S. Grimme, Semiempirical GGA-type density functional constructed with a long-range dispersion correction, Journal of Computational Chemistry, 27 (2006) 1787-1799.
[44] L. Bouëssel du Bourg, A.U. Ortiz, A. Boutin, F.-X. Coudert, Thermal and mechanical stability of zeolitic imidazolate frameworks polymorphs, APL Materials, 2 (2014) 124110.

Acknowledgments

We thank Kiyofumi Nitta and Oki Sekizawa for providing assistance on the setup for XAFS measurements under proposal No. 2018A1760 at BL05XU, Spring-8, Japan.

Funding: This work was supported by Natural Science Foundation of China (Grant Nos. 52090020, 11874076). A.K. thanks the Institute of Solid State Physics, University of Latvia as the Center of Excellence has received funding from the European Union's Horizon 2020 Framework Programme H2020-WIDESPREAD- 01-20l6-2017-Teaming Phase2 under grant agreement No. 739508, project CAMART2. M.T.L. thanks the financial support from the Natural Science Foundation of China (Grant No. 11804011).

Author contributions: S.S. and L.W. conceived the project. S.S. and L.W. designed and performed the electrical transport, XRD, and Raman experiments and analyzed the data. A.S.N. performed theoretical band-structure calculations. R.B. prepared nanowire samples for the experiments and performed TEM data analysis.
M.T.L. collected XAS data at beamline. A.K. and S.S. conducted XAS data analysis. S.S., A.S.N., A.K., L.W., Y.J.T. and H-K.M. wrote the manuscript with inputs of all the authors.

Competing interests: The authors declare that there is no conflict of interests.

Figures and Tables

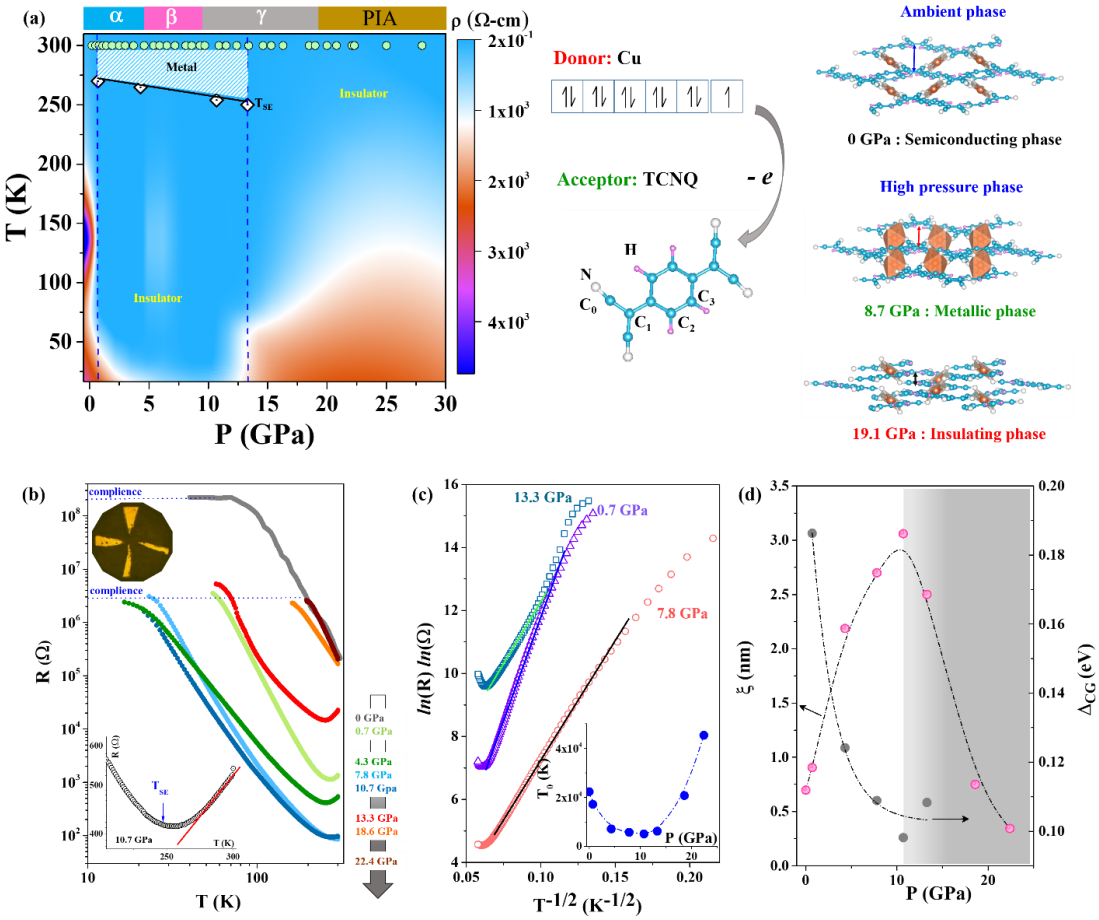

Fig. 1. (Color online) Phase-temperature phase diagram of Cu-TCNQ and resistivity profiles. (a) Pressure-temperature (*P-T*) phase diagram consisting of three different electronic phases in Cu-TCNQ, namely semiconducting (ambient) (left), metallic (8.7 GPa), and insulating (19.1 GPa) phases (top right). The metal donor atom Cu and acceptor TCNQ molecules form Cu-TCNQ stacks (top left). The white squares are the positions of the kinks (T_{SE}) in resistivity profiles shown in **(b)** which correspond to the semiconductor-metal transition temperatures. The green solid circles indicate the pressure-dependent resistivity data at ambient temperature. α, β, γ, and pressure-induced amorphization (PIA) correspond to four crystallographic phases at ambient temperature. **(c)** The ESVRH model fitting for *R-T* curves for few pressure points along with the pressure evolution of **(d)** ξ and Δ_{CG} (see text).

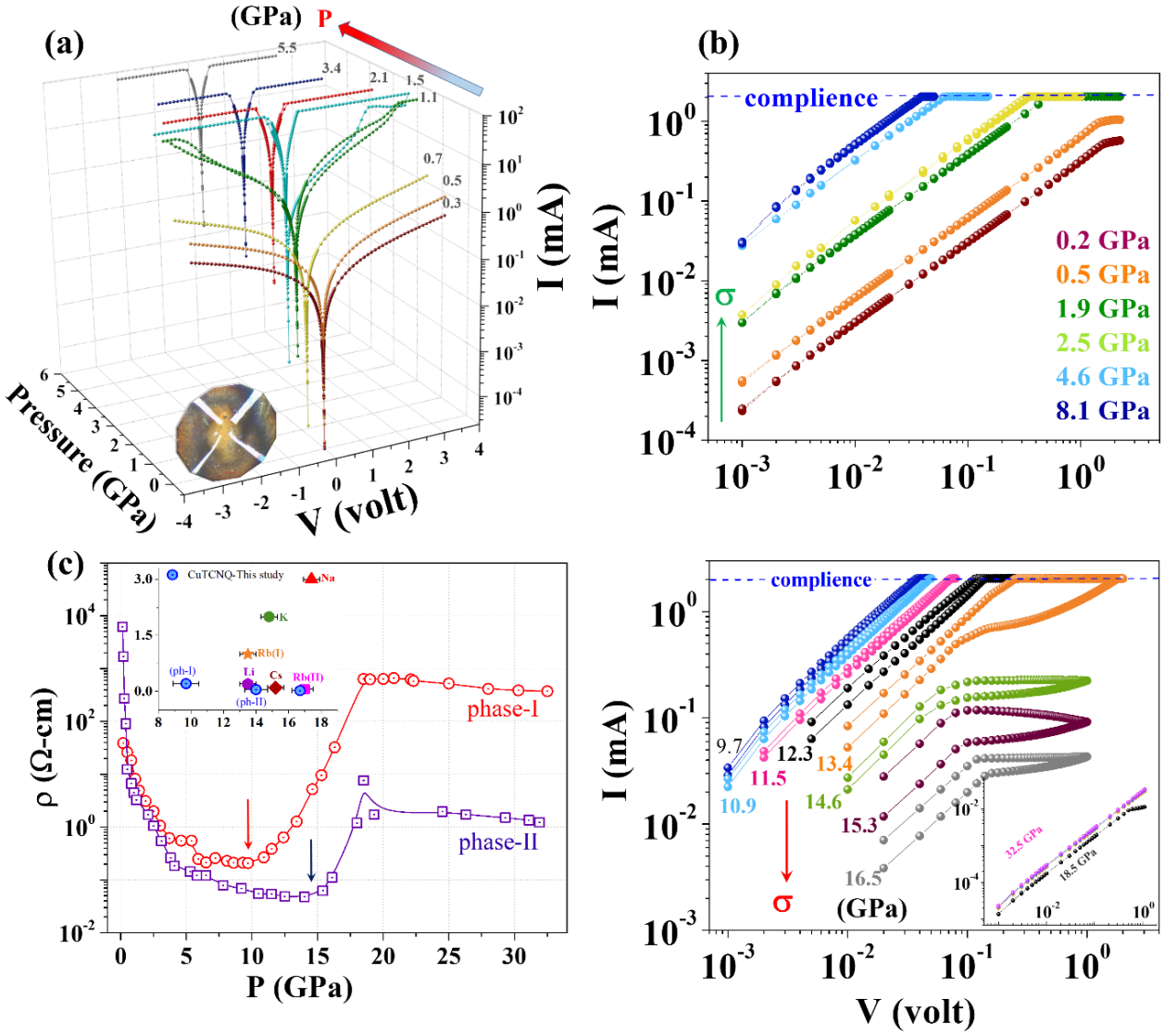

Fig. 2. (Color online) Pressure-dependent non-linear conductivity of Cu- TCNQ at room temperature. (a) characteristics show non-linear conductivity including HRS-LRS switching of under compression. The conductivity (σ) first **(b)** increase (top panel) and then decrease (bottom panel) with pressure. **(c)** Pressure dependencies of resistivity for phase-I and phase-II. Inset shows the observed lowest transition pressures for Cu-TCNQ in comparison with other alkali metal-TCNQ crystals. The molecular arrangement of Cu-TCNQ in the *ab*-plane is shown.

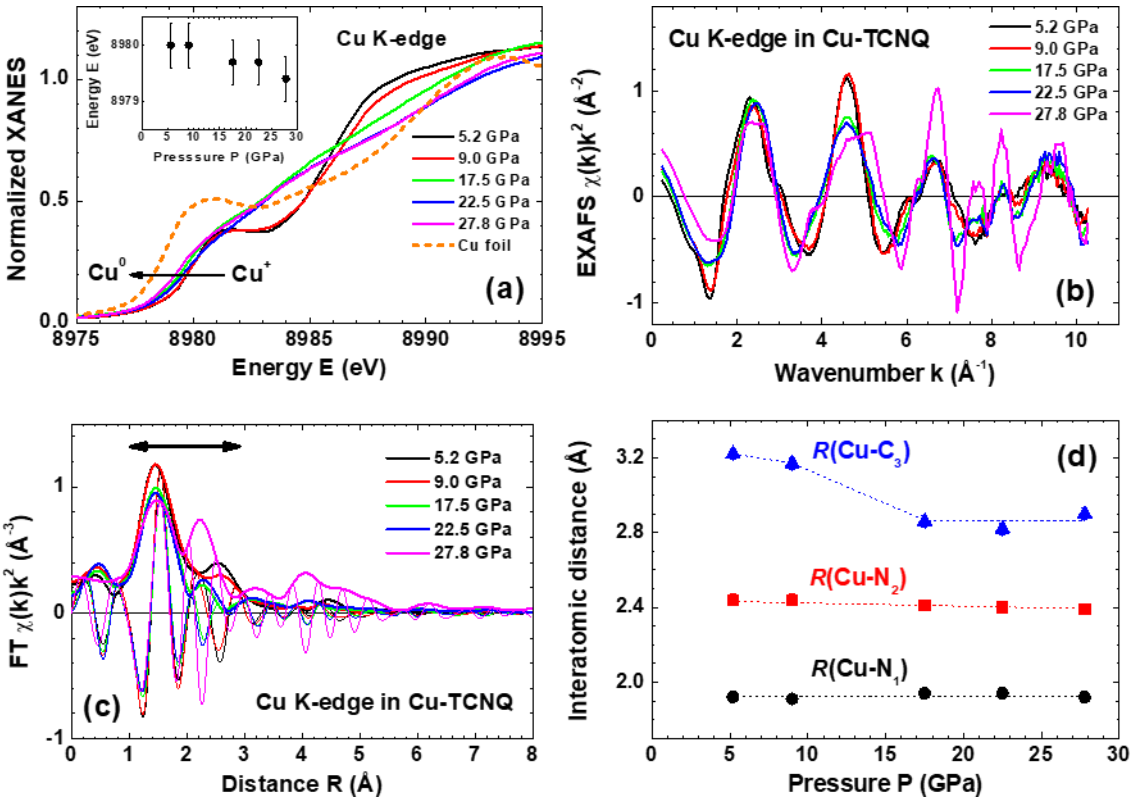

Fig. 3. (Color online) X-ray absorption spectroscopy under pressure. **(a)** Normalized Cu K-edge X-ray absorption near-edge structures (XANES) for Cu-TCNQ and Cu foil. Inset shows the pressure dependence of the absorption edge position determined as a first derivative of the absorption coefficient. The Cu K- edge EXAFS spectra **(b)** and their Fourier transforms (moduli and imaginary parts) **(c)** for Cu-TCNQ at different pressures. Note that the position of peaks in FTs differs from the true crystallographic values due to the presence of the scattering amplitude and phase shift contributions in the EXAFS spectra. The range of data analysis is indicated in (c) by the arrow. **(d)** Pressure dependence of the average interatomic distances R(Cu-N_1), R(Cu-N_2) and R(Cu-C_3). Dotted lines are guides for the eye.

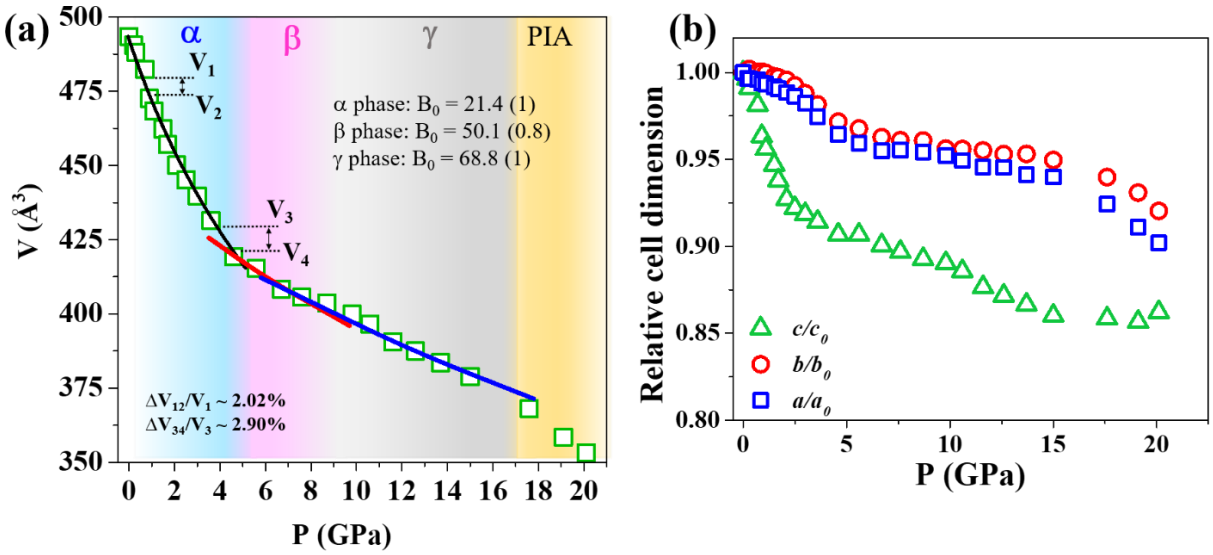

Fig. 4. (Color online) Structural transition under pressure. (a) Unit cell volume vs. pressure plot for α-, β-, and γ-phases fitted with second-order Birch-Murnaghan equation of state (solid lines). The low elastic modulus and their pressure-induced softening establish a direct correlation between instability and PIA [44]. **(b)** Evolution of the normalized lattice parameters show anisotropic compression of unit cells.

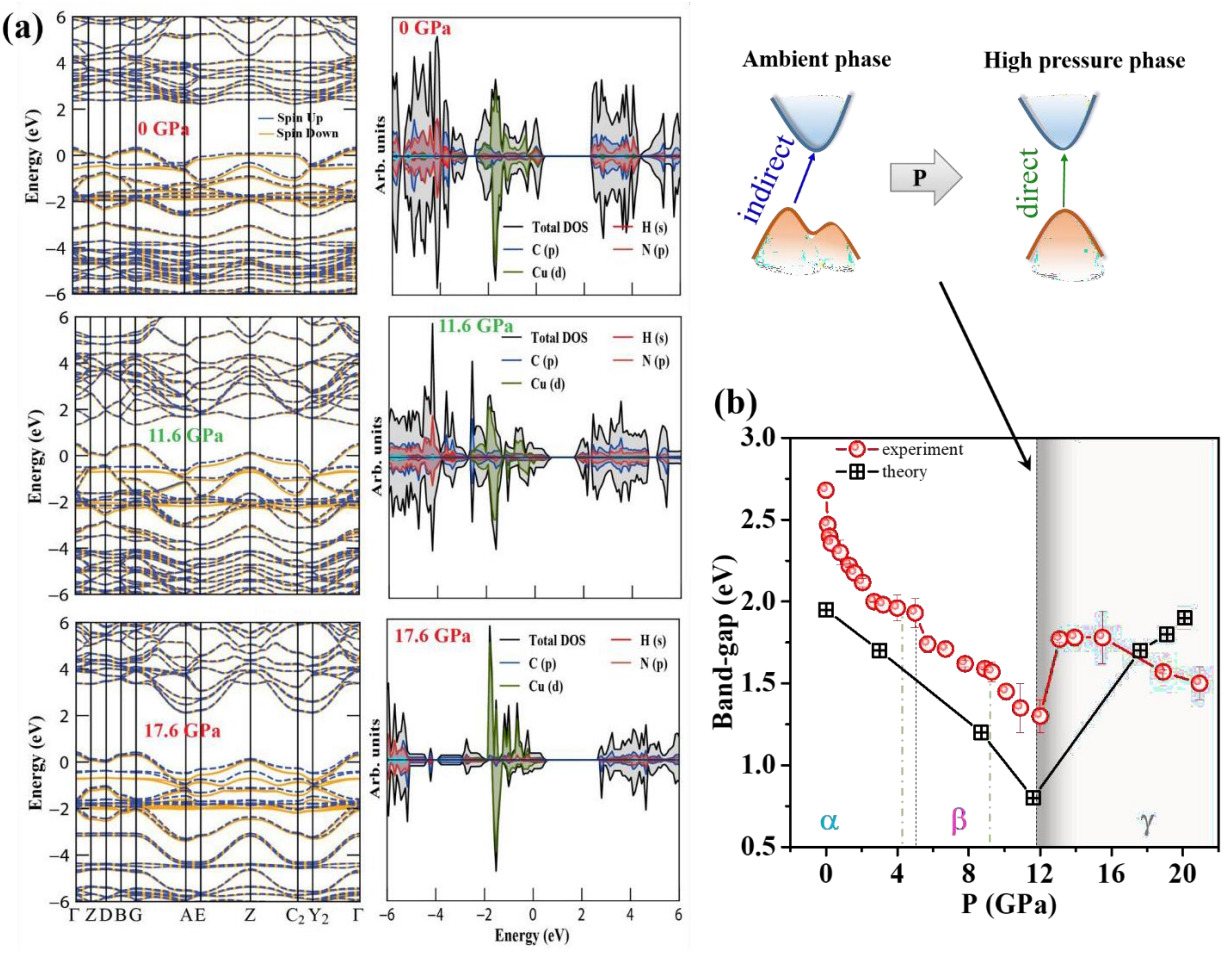

Fig. 5. (Color online) Evolution of band structure with pressure. (a) Calculated PDOS on each atom in Cu-TCNQ and the corresponding band structures at few representative pressure values. At ambient pressure, the calculated energy gap between VBM and CBM is 1.95 eV, which is slightly less than experimental value (2.6 eV) due to the unavoidable underestimations of the band gap by GGA (DFT-PBE) exchange-correlation functionals. **(b)** The optical band gap derived from the experimental absorption data is compared with the theoretical indirect/direct band gap as a function of pressure. Green dashed lines show the structural phase transitions as derived from XRD data and lower than the values obtained from band gap calculations (black dotted lines).

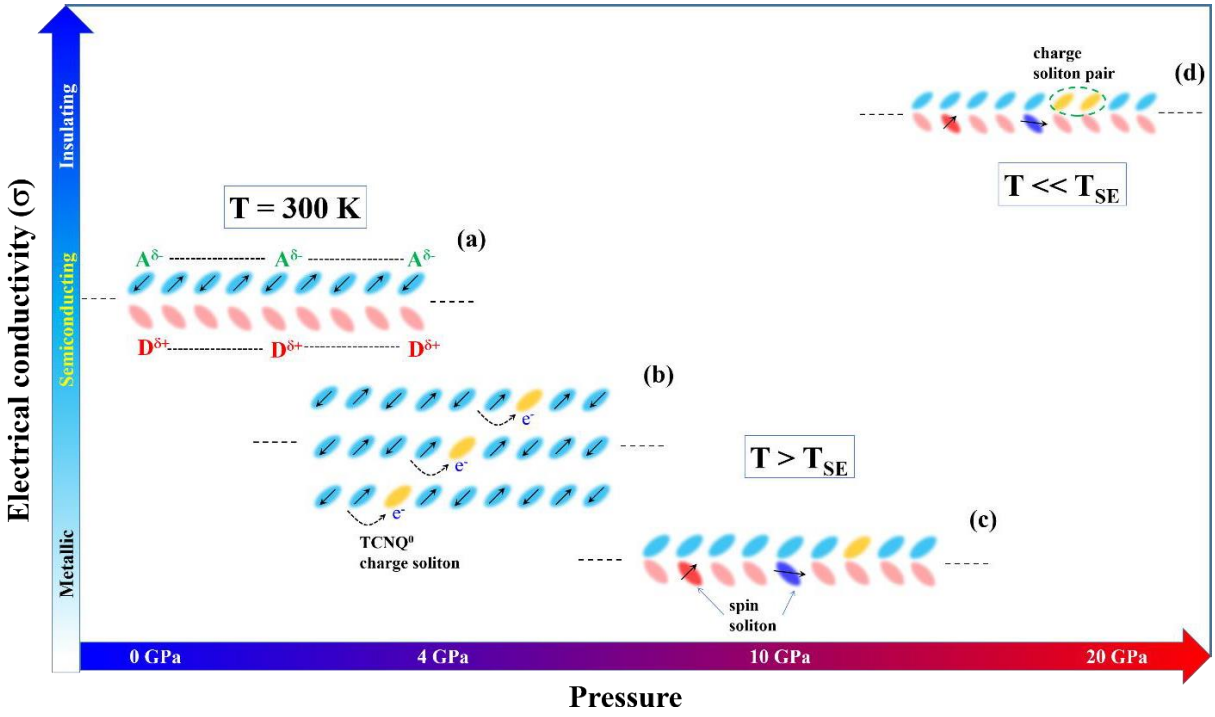

Fig. 6. (Color online) Topological excitations (solitons) and electrical conductivity evolution under compression. (a) D-A segregated stacking with partial charge transfer support semiconducting nature of Cu-TCNQ at ambient conditions. **(b)** For $T>T_{SE}$**,** at low pressure, few charge solitons propagate in organic stacks. **(c)** Around 10 GPa, charge and spin solitons become highly active and a metallic state emerges. **(d)** The soliton pairs are restricted to hop in the adjacent stacks and compels the system to return in an insulating state at very low temperatures and at high pressure.

SUPPLEMENTARY MATERIALS

Section S1: Electrical Resistive State Switching (ERSS) mechanism

Current-voltage ($I-V$) characteristics in Fig. S1(a) demonstrate that the conductivities for both phases (I and II) gradually increase as pressure increases. For a critical pressure $P_c = 1.1$ GPa (phase-I) and positive (negative) voltage sweep, current rapidly switches from an OFF-state (HRS) to an ON-state (LRS) at a threshold voltage V_{SET} (V_{RESET}) After switching, the current attains the compliance current limit. With reducing bias voltage, the sample returns to the HRS following a hysteresis path. Such ambipolar switching is qualitatively similar to the earlier results of a single nanowire device of Cu-TCNQ, but differs from its thin films and nanobridges. Fig. S1(b) shows a similar ON-OFF switching phenomenon with a relatively low pressure ~ 0.5 GPa is recorded for phase-II as well.

The platinum-MOF (Pt/Cu-TCNQ) band-diagram controls the resistive switching under pressure ($P \leq P_c$) where Cu-TCNQ has a suitable band-gap of 2.2-2.7 eV and Pt has the work-function 4 eV. The difference between the energy levels of MOF and Pt creates the deep level traps and therefore, trap-controlled space-charge-limited conduction (SCLC) mechanism fits well (solid red line in Fig. 2(a)). For low applied bias, $I-V$ relationship obeys Ohmic conduction ($I \propto V$) (solid blue lines in Fig. S1(a)) and thermally generated charge carriers participate in the conduction process. With higher applied bias (or, applied electric field), a non-equilibrium of charge carrier density sets in (SET and RESET) and $I-V$ characteristics change from Ohmic to SCLC ($I \propto V^2$) to trap-filled SCLC ($I \propto V^n, n > 2$) in nature.

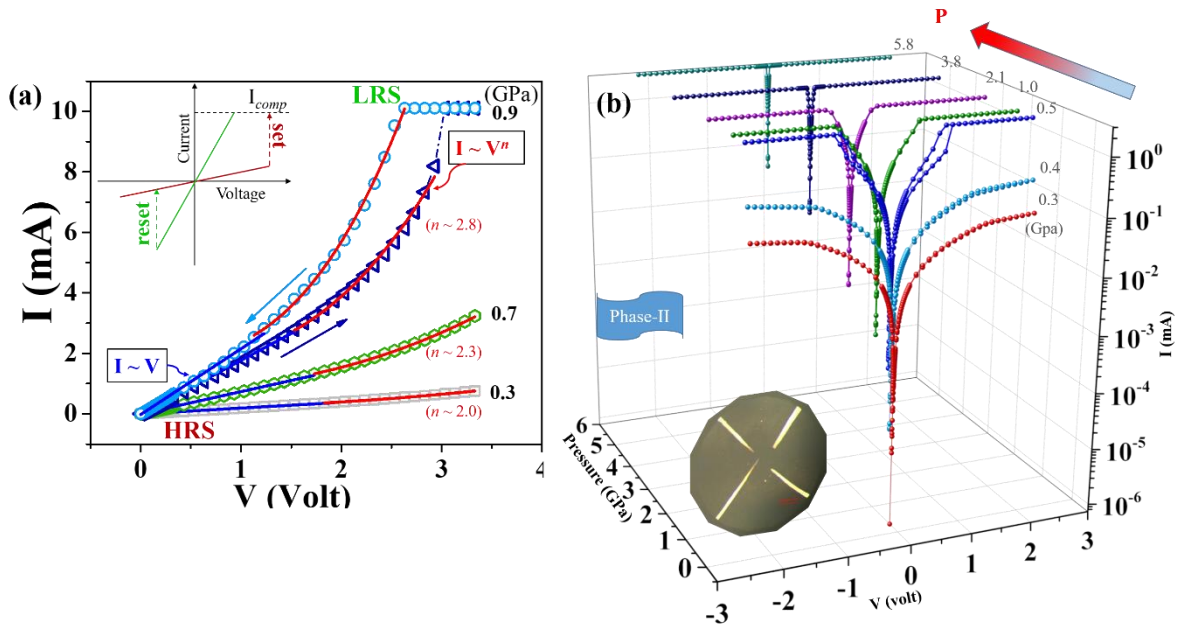

Fig. S1. (Color online) ERSS and current-voltage characteristics. (a) $I-V$ characteristics show HRS-LRS switching of phase-I under compression (see text). (b) Current-voltage characteristics of Cu-TCNQ phase-II at ambient temperature at few representative pressure values. There is a huge increment of current at 0.5 GPa and reaches its compliance limit.

Section S2: X-Ray diffraction and Raman spectroscopy studies under pressure at ambient temperature

Pressurization removes imperfections and disorders; while structural rearrangements allow CuTCNQ to form lower symmetric phases with a distortion of the framework or metal center coordination from ambient monoclinic *Pn* phase(*1*) ($a = b = 11.266$Å, $c = 3.8878$Å, $\alpha = \beta = \gamma = 90°$)(*1*) (Fig. S2). The typical synchrotron X-ray diffraction (XRD) data up to 30 GPa and the profile fits with the Le Bail refinements are displayed in Fig. S2(a) and Fig. S2(b) respectively. An initial compression leads to the sudden disappearance of (111) refection along with a volume collapse $\left(\frac{V_{12}}{V_1}\right)$ about 2% within α-phase around 1.0 GPa (dashed rectangle in Fig. S2(a)). The emergence of new peaks and change in lattice angle in Fig. S3 indicate that first structural transition around ~ 4.2 GPa from α → β phase ($\left(\frac{V_{34}}{V_3}\right)$ ~ 3%). The drastic changes in the crystal or electronic

structures(*2*) and the stabilization of lattice(*3*) around 4 GPa were predicted in previous studies also. Around 8.7 GPa, multiple splits of diffraction peaks corresponding to (112) and (023) reflections occur (arrows in Fig. S2).

The pressure dependencies of unit cell parameters including volume are shown in Fig. 4(a) and Fig. 4(b) respectively. The compression-induced stiffening of Cu-TCNQ was fitted with the second-order Birch-Murnaghan equation of state (EOS) (solid lined in Fig. 4(a)). The bulk-moduli B_0 of α-, β-, and γ-phase are 21.4(1), 50.1(0.8), and 68.8(1) GPa respectively. The absence of any discontinuity in pressure-volume data (9-16 GPa) suggests a second-order phase transition from β $\rightarrow$ γ phases. Above 16 GPa, the peak intensities dramatically reduced and finally disappeared to set PIA (30 GPa).

While a and b axes lattice parameters decrease monotonically, c-axis exhibits a steep reduction with increasing pressure in α-phase (Fig. 4(b)) due to the ease of compression of π-stacks. However, as the in-plane C≡N bonds are closely packed, the structure may accommodate greater compression along $a - b$ planes resulting in an anisotropic compression in the lattice. While all the unit cell parameters continue to decrease monotonically in β-phase, a and b axes lattice parameters reduce sharply compared to c-axis in γ-phase. The overall structure is highly compressed and further volume reduction causes extreme distortions/destructions to the organic chains.

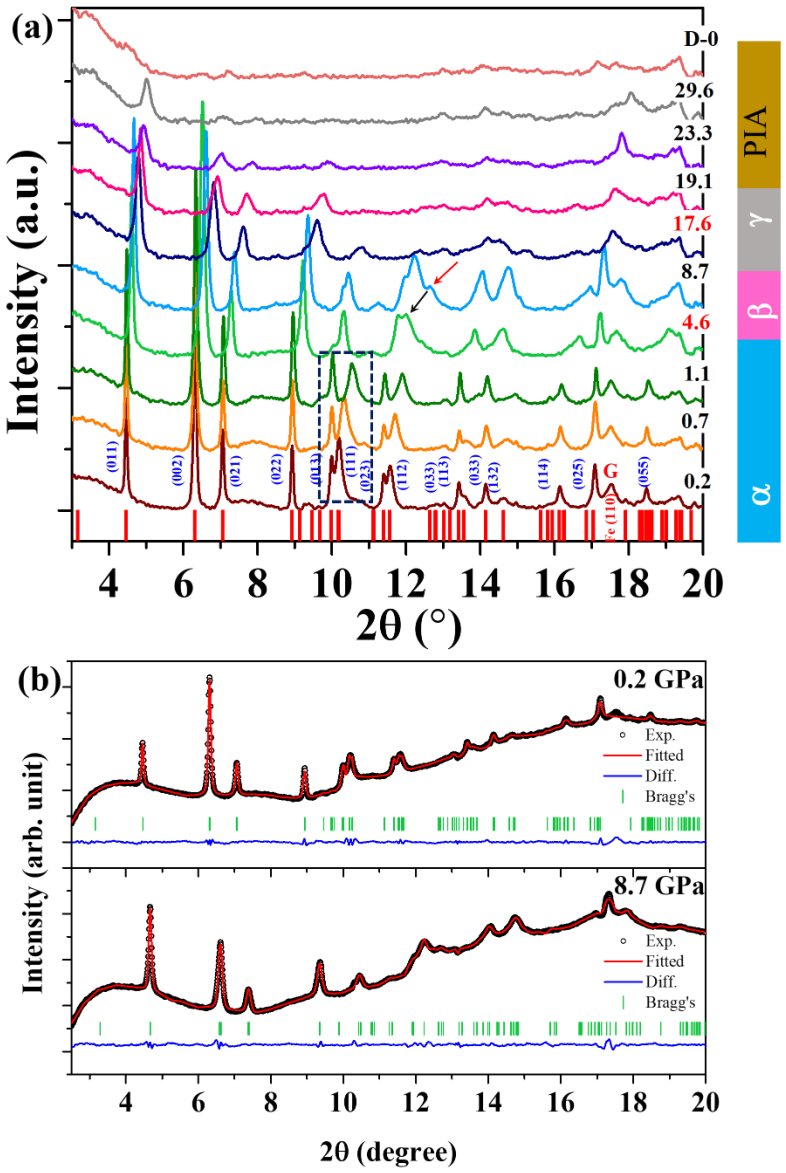

Fig. S2. (Color online) In-situ pressure-induced X-ray diffraction for phase-I at room temperature. (a) X-Ray diffraction patterns under compression show emergence before PIA. (b) XRD Le Bail profile fits for two representative pressure values.

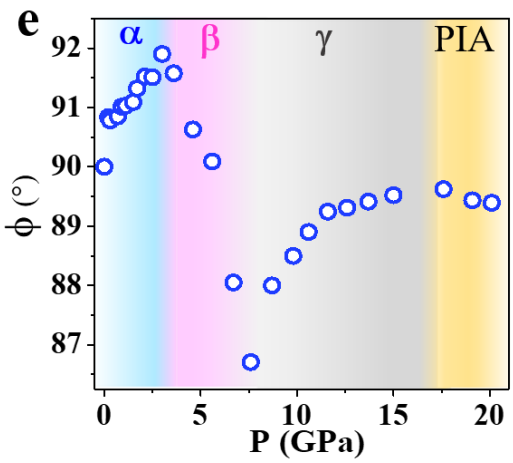

Fig. S3. (Color online) Pressure-induced variation of monoclinic angle. The variation of the monoclinic angle (ϕ) with pressure and reached to its maximum and minimum values around α → β and β → γ phase transitions respectively.

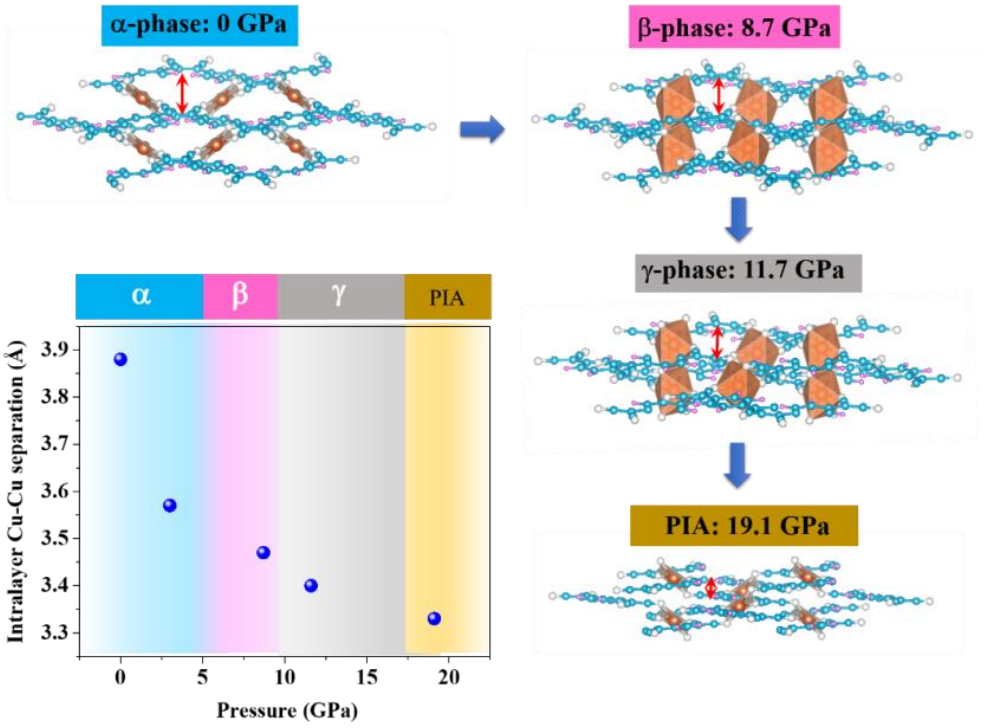

Fig. S4. (Color online) The evolution of intra-layer Cu-Cu separation with pressure. The evolution of crystal structure and intra-layer Cu-Cu separation with pressure show steep reduction in pore volume in Cu-TCNQ during compression.

At ambient conditions, the fundamental modes (1202, 1380, 1603, and 2203 cm^{-1}) corresponding to bending and stretching of organics atoms (C, N, H) are shown in Fig. S4 and are well consistent with previous investigation(*2*). All these modes hardened under pressure with different modality as clear from their different pressure dependencies (dv/dP). The modes like C=C-H bending and C-C≡N stretching modes demonstrated distinct changes around α→β phase transition. Moreover, the population of electrons in TCNQ increases with decreasing lengths of these two bonds.

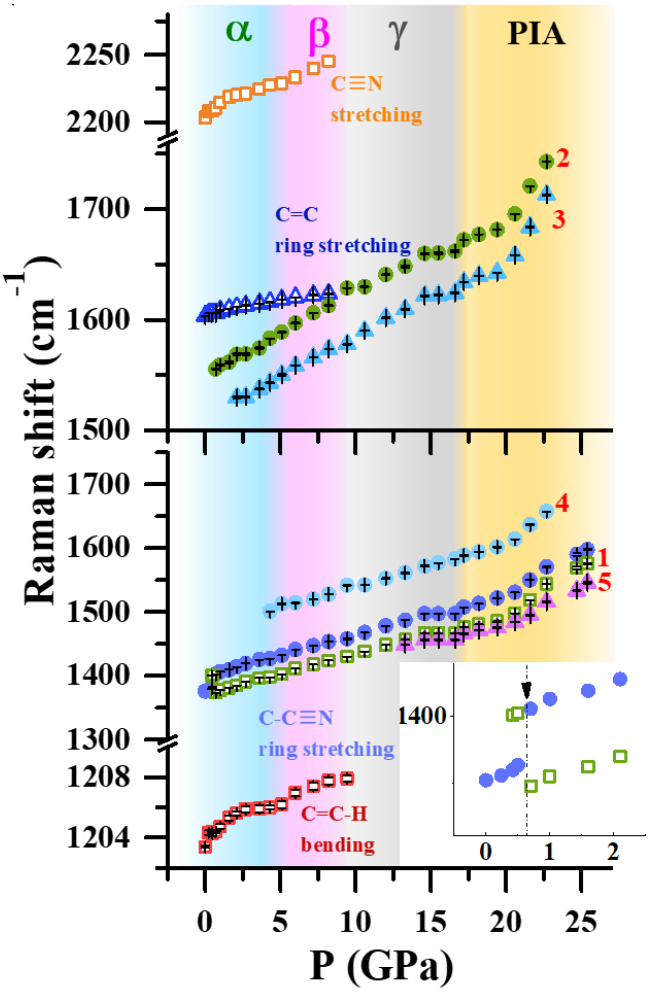

Fig. S5. (Color online) Pressure dependencies of phonon modes at room temperature. (a) Pressure dependencies of modes showing hardening under compression. Inset shows the resonance energy transfer of the C-C≡N mode.

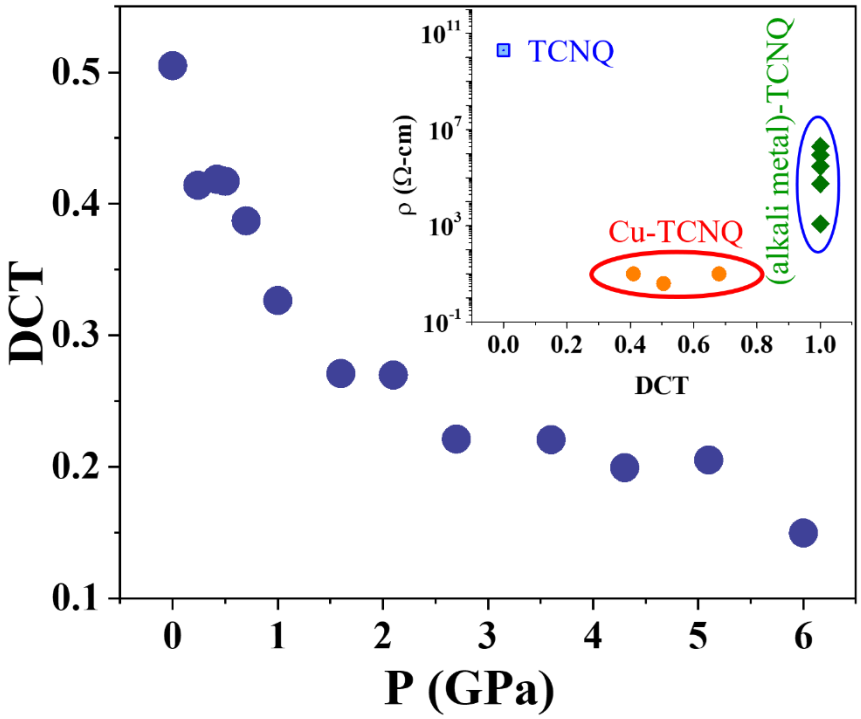

Fig. S6. (Color online) Pressure-induced change in degree of charge transfer. (a) Variation of DCT with pressure for Cu-TCNQ. Inset: DCT vs. resistivity plot for TCNQ and its salts. While alkali metal-TCNQ compounds have perfect DCT = 1 have very low conductivity, Cu-TCNQ nanowires including thin films have high conductivity with partial charge transfer.

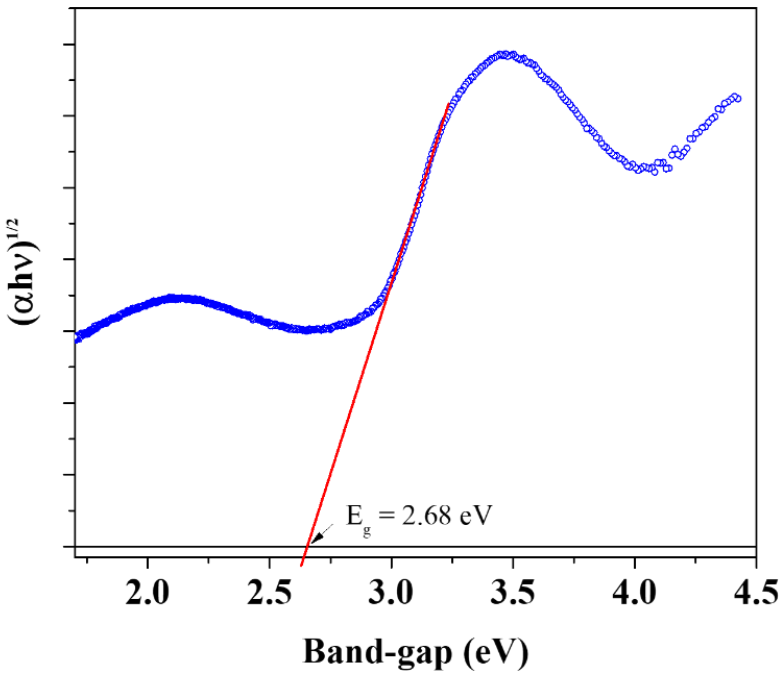

Fig. S7. Optical band-gap at ambient condition. The UV-vis absorption spectra of Cu-TCNQ at ambient condition with optical band-gap 2.68 eV.

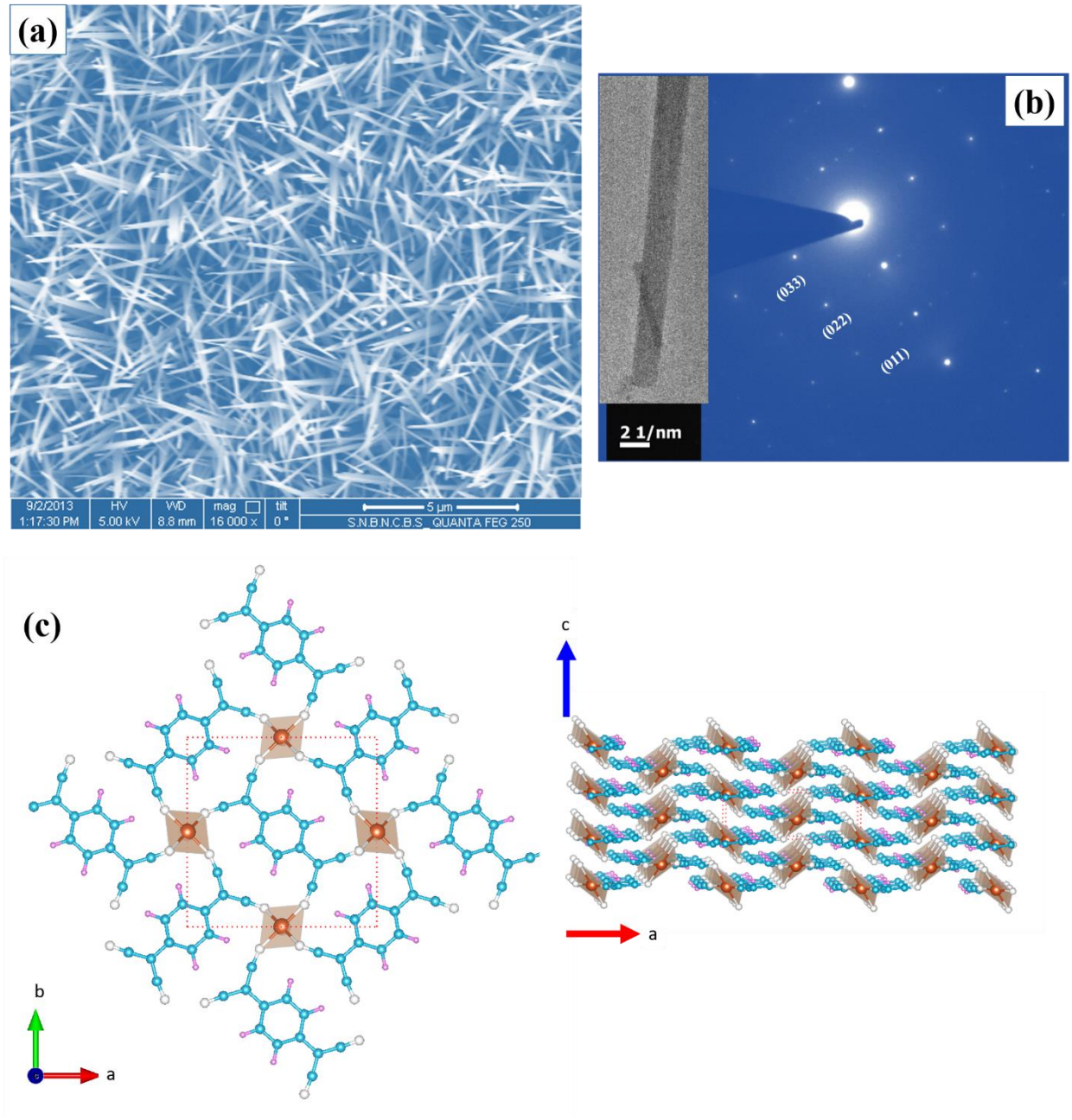

Fig. S8. (Color online) Electron microscopy images and molecular arrangements of Cu-TCNQ. (a) The SEM image of the as-grown phase-I nanowires with the diameter ranging from 20-50 nm. (b) HRTEM image shows single-crystalline nature of individual wire. (c) The molecular arrangement of the Cu-TCNQ and its stacking are shown (orange: Cu, cyan: C, white: N, and pink: H).

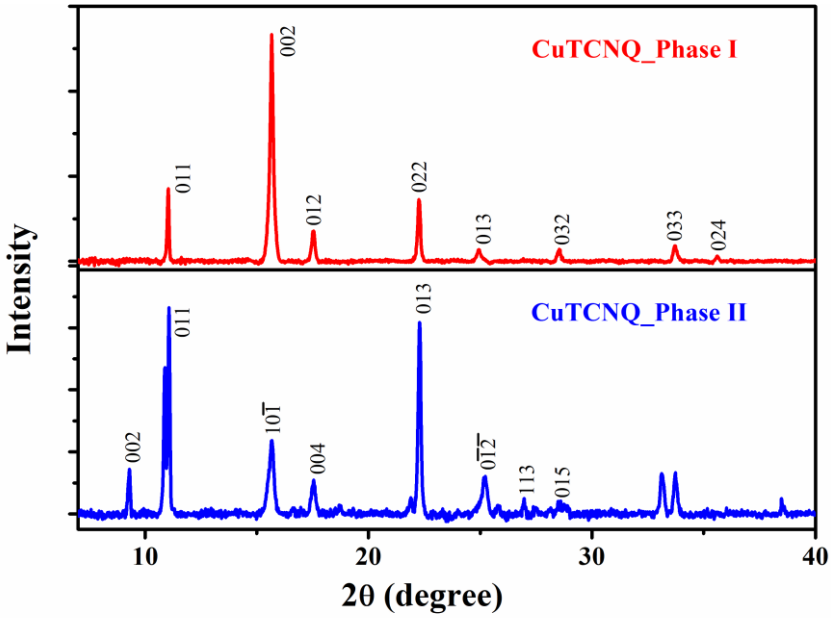

Fig. S9. (Color online) X-ray diffraction of two stable Cu-TCNQ phases. The x-ray diffraction patterns for CuTCNQ (a) phase-I and (b) phase-II were collected by CuK$_\alpha$ radiation.

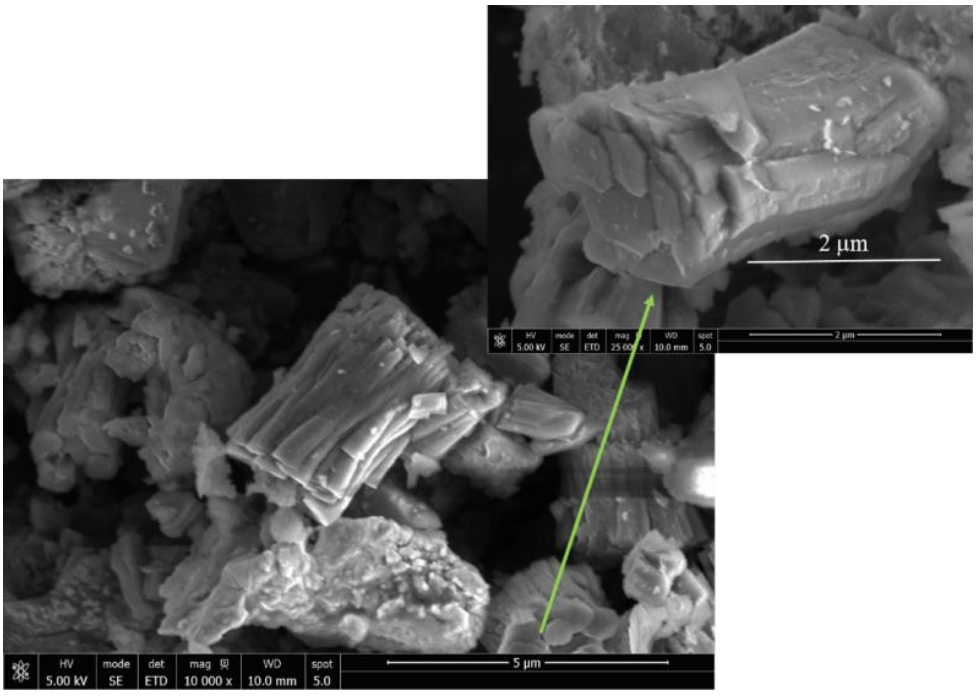

Fig. S10. (Color online) Electron microscopy image of recovered sample. SEM image of the pressure recovered (from 40 GPa) Cu-TCNQ sample at ambient temperature showing the change in packing density and increased dimensionality. It also demonstrate that nanowires lost their crystallinity and bundled up.

Section S3: X-ray absorption spectroscopy under high pressure at room temperature

The high-pressure synchrotron X-ray absorption spectroscopy (XAS) experiments on Cu-TCNQ sample were performed in the pressure range of 0-28 GPa at the BL05XU beamline at SPring-8 synchrotron radiation facility. The Cu K-edge absorption spectra were collected in the transmission mode.

The XAS data were analyzed by ATHENA(*4*) and XAESA(*5*) programs. The EXAFS spectra (Fig. 5(b)) were defined as $\chi(k) = (\mu(k) - \mu_0(k))/\Delta\mu_0$ after background removal where k is the photoelectron wavenumber, $\mu_0(k)$ is a smoothly varying absorption background, and $\Delta\mu_0$ is the absorption edge-jump. Their Fourier transforms (FTs) were calculated using the 10% Gaussian window-function (Fig. 5(c)). The contribution from the nearest atoms (6N and 4C) around the absorbing copper was isolated by back-FT in the range of R = 0.8-3.0 Å and analyzed within the single-scattering harmonic approximation using the conventional EXAFS equation(*6*). The required backscattering amplitude and phase shift functions for Cu-N and Cu-C atom pairs were calculated using ab initio self-consistent real-space multiple-scattering FEFF8.50L code(*7, 8*). The scattering potential and partial phase shifts were calculated within the muffin-tin (MT) approximation(*7, 8*) for the cluster with a radius of 8 Å constructed based on Cu-TCNQ crystallographic structure(*9*) and centered at the absorbing Cu atom. The photoelectron inelastic losses were accounted for within the one-plasmon approximation using the complex exchange-correlation Hedin-Lundqvist potential. The amplitude reduction factor S_0^2 is included in the scattering amplitude(*7, 8*), calculated by the FEFF code, and no additional correction of the EXAFS amplitude was performed. Due to a short range of the experimental EXAFS spectra, limited by glitches from the DAC cell, the fitting of the nearest atom contribution was performed in the *k*-space range of 1.7-8.0 $Å^{-1}$ using the three-component model(*10*). The model included three contributions due to Cu-N_1, Cu-N_2 and Cu-C_3 sub-shells (Fig. 6). The coordination numbers were constrained by the Cu-TCNQ structure, i.e. $N(N_1)$=4, $N(N_2)$=2 and $N(C_3)$=4, whereas three interatomic distances (R) and three mean-square

relative displacements (MSRDs) (σ^2), also known as the Debye-Waller factors, were set as variable parameters.

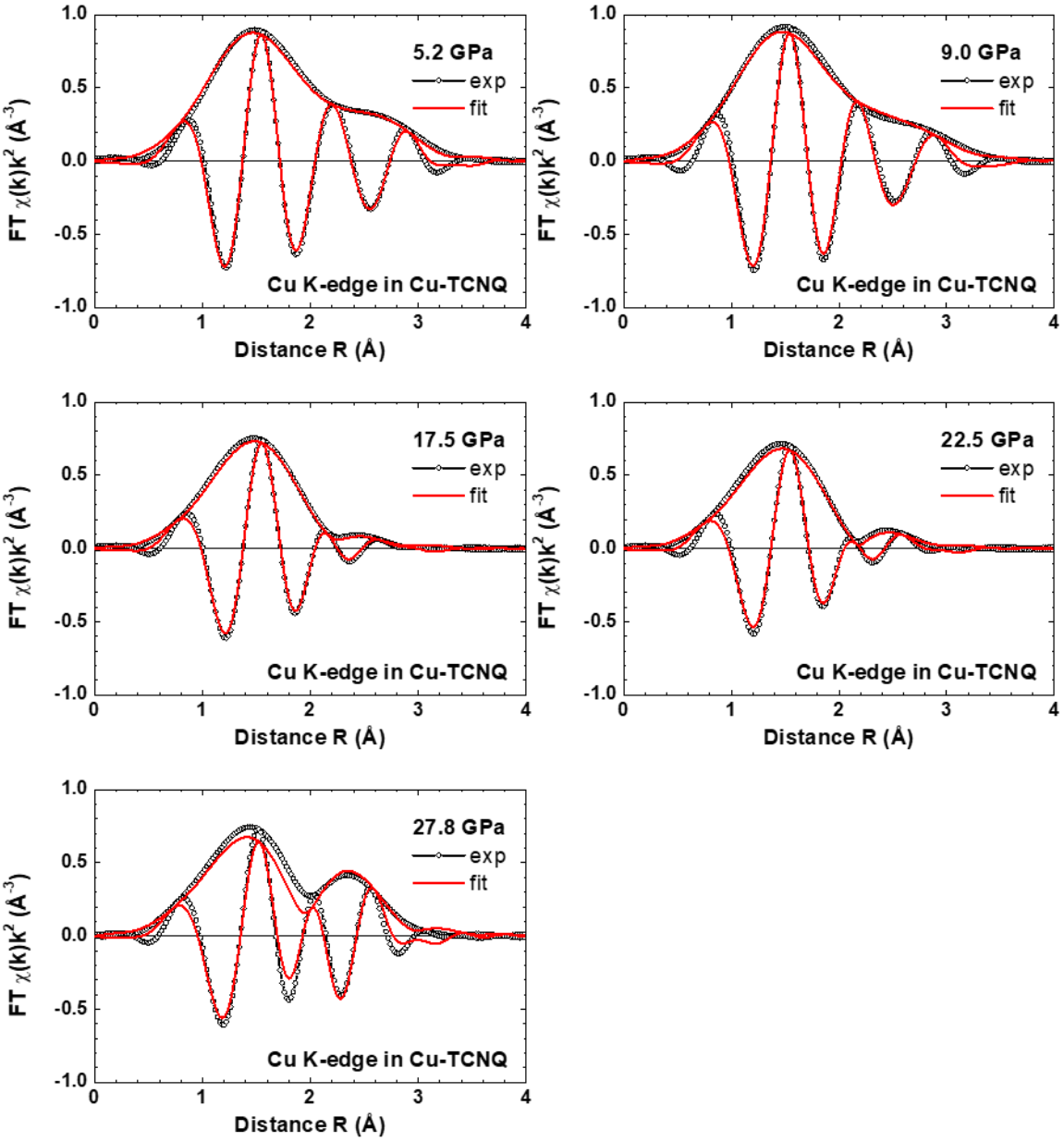

Fig. S11. (Color online) Fast Fourier transformation of Cu-K edge EXAFS spectra. Comparison of the Fourier transforms (moduli and imaginary parts) of the experimental (open circles) and best-fit (solid lines) Cu K-edge EXAFS spectra $k^2\chi(k)$ of Cu-TCNQ at different pressures.

References and Notes:

1. R. A. Heintz *et al.*, New Insight into the Nature of Cu(TCNQ): Solution Routes to Two Distinct Polymorphs and Their Relationship to Crystalline Films That Display Bistable Switching Behavior. *Inorganic Chemistry* **38**, 144-156 (1999).
2. Z. P. Hu *et al.*, High pressure Raman studies of 7,7,8,8-tetracyanoquinodimethane (TCNQ) and CuTCNQ. *Journal of Molecular Structure* **356**, 163-168 (1995).
3. R. Caputo, S. Demir, A. Tekin, First-Principles Crystal Structure Prediction of Cu(I)-TCNQ Polymorphs. *The Journal of Physical Chemistry C* **124**, 70-82 (2019).
4. B. Ravel, M. Newville, ATHENA, ARTEMIS, HEPHAESTUS: data analysis for X-ray absorption spectroscopy using IFEFFIT. *Journal of Synchrotron Radiation* **12**, 537-541 (2005).
5. A. Kalinko, XAESA v0.03. **https://github.com/aklnk/xaesa**, (2020).
6. A. Kuzmin, J. Chaboy, EXAFS and XANES analysis of oxides at the nanoscale. *IUCrJ* **1**, 571-589 (2014).
7. A. L. Ankudinov, B. Ravel, J. J. Rehr, S. D. Conradson, Real-space multiple-scattering calculation and interpretation of x-ray-absorption near-edge structure. *Physical Review B* **58**, 7565-7576 (1998).
8. J. J. Rehr, R. C. Albers, Theoretical approaches to x-ray absorption fine structure. *Reviews of Modern Physics* **72**, 621-654 (2000).
9. M. J. Capitan, J. Alvarez, F. Yndurain, Organometallic MTCNQ films: a comparative study of CuTCNQ versus AgTCNQ. *Physical Chemistry Chemical Physics* **20**, 21705-21715 (2018).
10. L. Hedin, B. I. Lundqvist, Explicit local exchange-correlation potentials. *Journal of Physics C: Solid State Physics* **4**, 2064-2083 (1971).

Highlights

- A comprehensive study of low-temperature and high-pressure induced electrical conductivity of CuTCNQ explores the concept of topological charge transport for the first time.
- The pressure-temperature phase diagram containing three distinct electronic states like semiconducting, metallic, and insulating phases for CuTCNQ has been presented.
- *In-situ* x-ray absorption spectroscopy of the metal establishes the high electrical conduction by the topological charges for the first time in this compound.
- Spin-polarized density functional theory (DFT) calculations and experimental optical absorption spectroscopy captured a pressure-driven indirect to direct band gap transition in CuTCNQ at ambient temperature.

Author contributions: S.S. and L.W. conceived the project. S.S. and L.W. designed and performed the electrical transport, XRD, and Raman experiments and analyzed the data. A.S.N. performed theoretical band-structure calculations. R.B. prepared nanowire samples for the experiments and performed TEM data analysis. M.T.L. collected XAS data at beamline. A.K. and S.S. conducted XAS data analysis. S.S., A.S.N., A.K., L.W. and H-K.M. wrote the manuscript with inputs of all the authors.

Competing interests: The authors declare that there is no conflict of interests.